

Broadband X-ray spectral variability of the pulsing ULX NGC 1313 X-2

A. Robba^{*1,2}, C. Pinto², D. J. Walton³, R. Soria^{4,5}, P. Kosec^{3,13}, F. Pintore², T. P. Roberts⁶, W. N. Alston³, M. Middleton⁷, G. Cusumano², H. P. Earnshaw⁸, F. Fürst⁹, R. Sathyaprakash^{6,12}, E. Kyriasis^{10,11}, and A. C. Fabian³

¹ Università degli Studi di Palermo, Dipartimento di Fisica e Chimica, via Archirafi 36, I-90123 Palermo, Italy

² INAF/IASF Palermo, via Ugo La Malfa 153, I-90146 Palermo, Italy

³ Institute of Astronomy, Madingley Road, CB3 0HA Cambridge, UK

⁴ College of Astronomy and Space Sciences, University of the Chinese Academy of Sciences, Beijing 100049, China

⁵ Sydney Institute for Astronomy, School of Physics A28, The University of Sydney, Sydney, NSW 2006, Australia

⁶ Centre for Extragalactic Astronomy, Department of Physics, Durham University, South Road, Durham DH1 3LE, UK

⁷ Department of Physics and Astronomy, University of Southampton, Highfield, Southampton SO17 1BJ, UK

⁸ Cahill Center for Astronomy and Astrophysics, California Institute of Technology, Pasadena, CA 91125, USA

⁹ Science Operations Department, European Space Astronomy Centre (ESA/ESAC), Villanueva de la Canada, 28692, Madrid, Spain

¹⁰ University of Crete, Department of Physics, GR-71003, Heraklion, Greece

¹¹ Institute of Astrophysics, FORTH, GR-71110 Heraklion, Greece

¹² Institut de Ciències de l'Espai, Carrer de Can Magrans, 08193 Cerdanyola del Vallès, Barcelona

¹³ MIT Kavli Institute for Astrophysics and Space Research, Cambridge, MA 02139, USA

Received ?; Accepted ?

ABSTRACT

Context. It is thought that ultraluminous X-ray sources (ULXs) are mainly powered by super-Eddington accreting neutron stars or black holes as shown by the recent discovery of X-ray pulsations and relativistic winds.

Aims. This work presents a follow-up study of the spectral evolution over two decades of the pulsing ULX NGC 1313 X-2 in order to understand the structure of the accretion disc. The primary objective is to determine the shape and nature of the dominant spectral components by investigating their variability with the changes in the source luminosity.

Methods. We performed a spectral analysis over the canonical 0.3–10.0 keV energy band of all the high signal-to-noise *XMM-Newton* observations (96% of the available data), and we tested a number of different spectral models, which should approximate super-Eddington accretion discs. The baseline model consists of two thermal blackbody components with different temperatures plus an exponential cutoff powerlaw.

Results. The baseline model provides a good description of the X-ray spectra. In particular, the hotter and brighter ($L_X \sim 6\text{--}9 \times 10^{39}$ erg s^{-1}) thermal component describes the emission from the super-Eddington inner disc and the cutoff powerlaw describes the contribution from the accretion column of the neutron star. Instead, the cooler component describes the emission from the outer region of the disc close to the spherisation radius and the wind. The luminosity-temperature relation for the cool component follows a negative trend, which is not consistent with $L \propto T^4$, as is expected from a sub-Eddington thin disc of Shakura-Sunayev. This is not consistent with $L \propto T^2$ either, as is expected for an advection-dominated disc. However, this would rather agree with a wind-dominated X-ray emitting region. Instead, the (L_X, T_{disk}) relation for the hotter component is somewhere in between the first two theoretical scenarios.

Conclusions. Our findings agree with the super-Eddington scenario and provide further detail on the disc structure. The source spectral evolution is qualitatively similar to that seen in NGC 1313 X-1 and Holmberg IX X-1, indicating a common structure and evolution among archetypal ULXs.

Key words. Accretion, accretion discs – X-rays: binaries – X-rays: individual (NGC 1313 X-2)

1. Introduction

Ultraluminous X-ray sources (ULXs) are among the best candidates for studying super-Eddington accretion in stellar-mass accreting compact objects. ULXs are the brightest off-nuclear, steady, point-like X-ray sources ($> 10^{39}$ erg s^{-1}) in the Universe. They are often found in or near regions of recent star formation (Swartz et al. 2009; Kovelakas et al. 2020) and they have X-ray luminosities that exceed the isotropic Eddington luminosity for a standard black hole (BH) with a mass of $M \approx 10 M_\odot$ (e.g. Kaaret et al. 2017). ULXs represent a heterogeneous sample of astronomical sources and are composed of a compact object, most

likely a BH or a NS, and a companion star, which has been found to be a red or blue supergiant in some ULXs, see for example Heida et al. (2019).

In order to explain the high X-ray luminosities of these sources, several hypotheses have been proposed. A first scenario suggests that ULXs are powered by stellar-mass BHs whose radiation is preferentially beamed in our line of sight (King et al. 2001; Poutanen et al. 2007). A second scenario supposes that a BH more massive than $10 M_\odot$ (30–80 M_\odot ; e.g. Zampieri & Roberts 2009), which accretes at or below the Eddington limit, is the compact object of a ULX. The existence of more massive BHs was proven by the detection of gravitational waves (e.g. Abbott et al. 2016a,b; Abbott et al. 2019, with BH masses between

* alessandra.robba@inaf.it

$10 M_{\odot}$ and $80 M_{\odot}$. In addition, in the past, other theories have suggested that some of these systems could be intermediate-mass BHs ($10^{3-4} M_{\odot}$, Colbert & Mushotzky 1999), accreting at sub-Eddington rates from low-mass companion stars with ESO243-49 HLX-1 being the best candidate (see Farrell et al. 2009).

For many years, the mass estimation of putative BHs powering ULXs was the subject of significant debate. However, the recent detection of coherent pulsations in several sources clearly demonstrates that some ULXs are powered by NSs accreting at very high Eddington rates with luminosities up to $\sim 500 L_{\text{Edd}}$. The first pulsation in a ULX was discovered in M82 X-2 by Bachetti et al. (2014) with *NuSTAR* observations and, at the moment, six ULXs are known to exhibit pulsations (Israel et al. 2017a,b; Fürst et al. 2016; Carpano et al. 2018; Sathyaprakash et al. 2019). It is not straightforward as to how to distinguish between BH and NS accretors based on the spectral analysis alone (Pintore et al. 2017; Koliopanos et al. 2017; Walton et al. 2018c). Moreover, pulsations are not always detectable; high count rates are indeed required for a low pulsed fraction or long exposure times for low count rates. This means that NSs are likely numerous among the compact objects of ULXs (see also Rodríguez Castillo et al. 2020; Wiktorowicz et al. 2019; King et al. 2017; Middleton & King 2016).

One of the fundamental predictions of the super-Eddington accretion theory is that strong, relativistic winds are launched from the supercritical discs, driven by the extreme radiation pressure (see e.g. Poutanen et al. 2007). Middleton et al. (2014) suggest that the spectral residuals around 1 keV could be associated with the winds. The first discovery of powerful winds in two ULXs was achieved by Pinto et al. (2016) by detecting blueshifted absorption lines in the high-resolution soft X-ray spectra provided by the *XMM-Newton* Reflection Grating Spectrometers (RGS). Further confirmations were obtained by Walton et al. (2016), Pinto et al. (2017), Kosec et al. (2018a) and Kosec et al. (2018b). The exact launching mechanism of such winds is still unclear as magnetic pressure might also contribute, although Pinto et al. (2020a) show that the relation between their velocities and ionisation parameters with the ULX luminosities agrees with the radiation driving mechanism. A thorough understanding of the ULX phenomenology requires additional constraints on the nature of these winds and their link with the source appearance and, therefore, accretion rate. This involves a study of the wind properties via high-resolution X-ray spectroscopy combined with a careful study of the evolution of ULX broadband spectra.

In this work we present the analysis of the X-ray spectra of the pulsating ULX X-2 in the galaxy NGC 1313. This barred galaxy (see Fig. 1) hosts a supernova remnant (SN 1978K) and two ULXs: X-1, close to the nucleus, and X-2, in the outskirts of the galaxy, which is the subject of this work. Sathyaprakash et al. (2019) discovered pulsations in NGC 1313 X-2 for the first time thanks to our deep *XMM-Newton* campaign. This ULX is characterised by strong variability in both luminosity and spectral shape. The high X-ray variability and spectral hardness suggest that the object is viewed at an inclination angle, which is low enough to allow for a direct view of the inner regions of its accretion flow and to detect pulsations (Middleton et al. 2015). NGC 1313 X-2 also shows evidence of winds in the form of X-ray spectral features in the soft band (see, e.g. Middleton et al. 2015 and Kosec et al. 2018a).

Throughout this work, we assume a distance of $D = 4.2$ Mpc to NGC 1313 (Mendez et al. 2002; Tully et al. 2016). The only

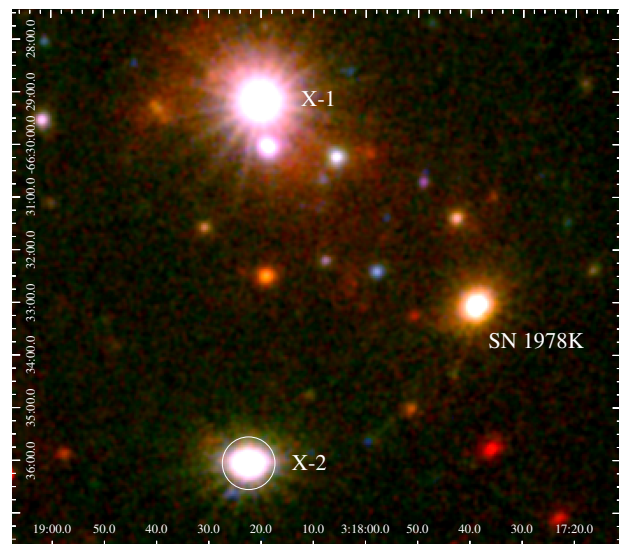


Fig. 1: *XMM-Newton* image of NGC 1313, which we obtained by combining all the data available from the 2017 EPIC-pn and MOS 1,2 observations. The $30''$ -radius circle around the ULX X-2 represents our default source extraction region. The red colour corresponds to 0.2–1 keV, green is for 1–2 keV, and blue is for 2–12 keV.

Cepheid distance available is 4.6 Mpc, which is a little bit of an outlier from the other measurements (Qing et al. 2015).

This paper is structured as follows. In Section 2, we provide details about the *XMM-Newton* observations used in this work and the data reduction. We show some basic time properties and the model-independent variability of the X-ray spectral shape. In Section 3, we describe the main results of the spectral and timing analysis, while in Section 4 we discuss the behaviour of the thermal components in the luminosity-temperature plane and, finally, provide our conclusions in Section 5.

2. Data analysis

2.1. Observations

We analysed the public archival *XMM-Newton* data of all the high signal-to-noise observations between 2000 and 2017. For our analysis, we particularly benefitted from a recent deep ~ 1 Ms view of NGC 1313 (PI: Pinto). The observations were carried out with the EPIC-pn and EPIC-MOS detectors (Strüder et al. 2001; Turner et al. 2001). For observations 0803990301 and 0803990401, we used only the data provided by pn and MOS 2 since the source was out of the MOS1 field of view due to damage to CCD6 and CCD3 (since 2005 and 2012, respectively). We have excluded observations 0150280201 and 0150280701 from this analysis as they contain only MOS data and they were very short, therefore providing low statistics. We also excluded observation 0205230201 because of a slew failure. Table 1 lists the details of the high signal-to-noise *XMM-Newton* observations (96% of the available data) that we analysed, including the date, the duration after the removal of flares, the count rates, and the filter of each observation.

Table 1: *XMM-Newton* observations of NGC 1313 X-2.

Obs.ID ⁽¹⁾	Date ⁽²⁾	Exposure time ⁽³⁾ (s)			Count rates ⁽⁴⁾ (cts/s)			Filter
		pn	MOS1	MOS2	pn	MOS1	MOS2	
0106860101	2000-10-17	31638	29250	29183	0.2554	0.07654	0.07588	Medium
0150280101	2003-11-25	19173	12498	12501	0.712	0.2181	0.2584	Thin1
0150280201	2003-12-09	5648	3609	3622	-	-	-	Thin1
0150280301	2003-12-21	10335	11971	11976	0.8365	0.2803	0.2795	Thin1
0150280401	2003-12-23	14098	15278	15293	0.9459	0.3081	0.3104	Thin1
0150280501	2003-12-25	15299	15262	15249	0.5249	0.1551	0.1510	Thin1
0150280601	2004-01-08	14757	15382	15377	0.4095	0.1277	0.1287	Thin1
0150280701	2003-12-27	16686	17779	17810	-	-	-	Thin1
0150281101	2004-01-16	7036	8671	8676	0.3545	0.1117	0.1170	Thin1
0205230201	2004-05-01	3459	12270	12275	-	-	-	Thin1
0205230301	2004-06-05	10036	11672	11674	0.9813	0.3181	0.32	Thin1
0205230401	2004-08-23	16137	17771	17776	0.2829	0.08781	0.09462	Thin1
0205230501	2004-11-23	14137	15769	15774	0.3190	0.09469	0.09883	Thin1
0205230601	2005-02-07	12437	14071	14074	0.9053	0.2974	0.3023	Thin1
0301860101	2006-03-06	19937	21570	21575	0.6510	0.1734	0.1963	Medium
0405090101	2006-10-15	121190	122456	122453	0.6437	0.1689	0.1576	Medium
0693850501	2012-12-16	123341	124921	124927	0.5395	0.1820	0.1819	Medium
0693851201	2012-12-22	123341	124921	124924	0.275	0.1036	0.1086	Medium
0722650101	2013-06-08	28841	30421	30426	0.1713	0.009892	0.01064	Medium
0742590301	2014-07-05	60040	61653	61624	0.3937	0.1074	0.1035	Medium
0742490101	2015-03-30	100041	98937	101625	0.07816	0.07223	0.07989	Medium
0764770101	2015-12-05	71941	73555	73524	0.2417	0.07106	0.07295	Thin1
0764770401	2016-03-23	30041	31653	31624	0.4102	0.1260	0.1261	Thin1
0782310101	2016-10-08	88041	89655	89626	0.5705	0.1863	0.1865	Medium
0794580601	2017-03-29	44542	46155	46127	0.3424	0.07281	0.1022	Medium
0803990101	2017-06-14	134142	133036	135725	0.2304	0.09635	0.09032	Medium
0803990201	2017-06-20	130841	132453	132425	0.3525	0.07631	0.08879	Medium
0803990301	2017-08-31	96686	-	91971	0.2380	-	0.07478	Medium
0803990401	2017-09-02	64008	-	63472	0.1077	-	0.09849	Medium
0803990701	2017-09-24	14500	9798	9797	0.2483	-	0.06602	Medium
0803990501	2017-12-07	125941	127555	127524	0.07091	0.07314	0.07887	Medium
0803990601	2017-12-09	125942	127555	127524	0.07893	0.07587	0.08123	Medium

Notes: ⁽¹⁾ observation identifier; ⁽²⁾ observation date (yyyy-mm-dd), ⁽³⁾ exposure time corrected for solar flares, ⁽⁴⁾ count rates in the 0.3–10 keV energy band.

2.2. Data reduction

The data analysis was performed using the *XMM-Newton Science Analysis System* (SAS) version 18.0.0 and the calibration files of January 2020.¹ Following the standard procedures, EPIC-pn and MOS data were reprocessed using the tasks *'epproc'* and *'emproc'*. The calibrated and concatenated event lists were filtered for high background epochs to acquire good time intervals (GTI) as follows. For each data set and each instrument, we extracted the high energy light curve (including events between 10–12 keV) to identify intervals of flaring particle background and we chose a suitable threshold (0.35 and 0.40 cts s⁻¹ for EPIC-MOS and pn, respectively), which is above the low steady background, to create the corresponding filtered EPIC event list. As recommended, we selected only single and double events (PATTERN ≤ 4) for EPIC-pn, and single to quadruple events (PATTERN ≤ 12) for EPIC-MOS.

We extracted EPIC MOS 1-2 and pn images in the 0.2–1/1–2/2–12 keV energy range and stacked them with the *'emosaic'* task. The field of the NGC 1313 galaxy and the brightest X-ray sources are shown in Fig. 1. We generally extracted source

spectra from circular regions with a radius of 30", except where the source was near the edge of the CCD (in these cases we used regions with a radius of 20") and the corresponding background from a larger circle in a nearby region on the same chip, free from contaminating point sources. The background region was also not generally placed in the Copper emission region (Lumb et al. 2002), with the exception of a small number of observations for which X-2 was also located in the Cu region.

We used the task *'arfgen'* to reproduce the effective area of the instrument and to correct instrumental factors, such as bad pixels and bad columns, using calibration information. The response matrix was generated with *'rmfgen'*. Since the EPIC-MOS1 and EPIC-MOS2 spectra are consistent for each observation, we stacked data from the MOS cameras into a single spectrum with the *'epicspeccombine'* routine.

2.3. Spectral analysis

Fig. 2 shows an overview of the spectral properties of X-2. In particular, the right panel illustrates the shape of the observed EPIC-pn spectra of NGC 1313 X-2 for six individual exposures during the most recent campaign (2017). The spectra in-

¹ <https://www.cosmos.esa.int/web/xmm-newton/ccf-release-notes>.

dicating substantial variability in luminosity by a factor of up to five and there is no significant spectral variability. The left panel of Fig. 2 instead shows a comparison between some spectra of a remarkably different shape and flux: a high flux spectrum (Obs.ID:0150280401), two spectra with intermediate flux (Obs.ID:0803990201 and Obs.ID:0782310101), and one with low flux (Obs.ID:0106860101). As it has been observed in most ULXs (e.g. Middleton et al. 2015), the spectrum becomes harder at higher fluxes. This behaviour disagrees with that seen in the classical Galactic X-ray binaries that accrete below Eddington limit and it is therefore considered as strong evidence in support of super-Eddington accretion. The left panel of Fig. 2 clearly shows that the spectrum is more variable in the hard X-ray band ($\gtrsim 1$ keV), which indicates that at least two different (soft and hard) spectral components are responsible for the X-ray emission.

We carried the spectral analysis out over the 0.3–10.0 keV energy range with XSPEC version 12.10.1 (Arnaud 1996). We simultaneously fitted the spectra of the MOS and pn cameras and estimated the parameter uncertainties at the 68% confidence level. Spectra were grouped for a minimum of 25 counts per energy bin, so that the χ^2 statistic could be used.

There is no coverage beyond 10 keV in most observations and even in the *NuSTAR* data, the source has low statistics above 10 keV (e.g. Bachetti et al. 2013). As the source is generally softer than X-1 in the NGC 1313 galaxy, the systematic error due to the lack of *NuSTAR* data is negligible. We therefore focussed on the canonical 0.3–10 keV X-ray band and assumed a simplified model with either two or three emission components. In the case, for instance, of the double blackbody disc and an exponential cutoff powerlaw model, the low-temperature component mimics the emission of the outer disc and wind, while the hotter temperature component reproduces the emission from the inner super-Eddington accretion flow. The third component is necessary to describe the contributions of the central accretion columns by the magnetic accretor, that is, the NS. Walton et al. (2018c) show that in all ULXs, this latter component is significant above 8–9 keV (see also Bachetti et al. 2013).

2.4. Timing analysis

In order to better understand our spectra, we extracted light curves in the whole band (0.3–10 keV) and in two different bands (i.e. soft 0.3–1.2 keV and hard 1.2–10 keV). The latter were extracted to calculate the hardness ratios (HRs), which were computed as follows:

$$HR = \frac{\text{Hard Rate}_{1.2-10\text{keV}}}{\text{Soft Rate}_{0.3-1.2\text{keV}} + \text{Hard Rate}_{1.2-10\text{keV}}}. \quad (1)$$

We chose to split the bands at 1.2 keV because this is the average energy at which the spectral curvature changes in the EPIC spectra (the case for Obs.ID:0803990201 is shown in Fig. 4). We plotted the full-band light curve colour-coded according to the HR in Fig. 3, where the vertical grey-dashed lines separate each observation.

NGC 1313 X-2 shows high variability during the two decades of (non-contiguous) observations. As a short-term flux variability test, we adopted the normalised excess variance in the whole band (0.3–10 keV), which is useful to quantify the different amplitudes of intrinsic variability of each light curve. As reported by Nandra et al. (1997), it is defined as follows:

$$\sigma_{NXV}^2 = \frac{1}{N\bar{x}^2} \sum_{i=1}^N [(x_i - \bar{x})^2 - \sigma_{err,i}^2], \quad (2)$$

where x_i and $\sigma_{err,i}$ are the count rate and its error in the i -th bin, \bar{x} is the mean count rate, and N is the number of bins used to estimate σ_{NXV}^2 . The associated error is the following:

$$\Delta\sigma_{NXV}^2 = \frac{S_D}{\bar{x}^2(N)^{1/2}},$$

$$S_D = \frac{1}{N-1} \sum_{i=1}^N \{[(x_i - \bar{x})^2 - \sigma_{err,i}^2] - \sigma_{NXV}^2 \bar{x}^2\}^2.$$

The fractional root mean square (RMS) variability amplitude (F_{var} , see Vaughan et al. 2003) is the square root of the normalised excess variance, that is

$$F_{var}(\%) = \sqrt{\sigma_{NXV}^2} \times 100 = \sqrt{\frac{1}{N\bar{x}^2} \sum_{i=1}^N [(x_i - \bar{x})^2 - \sigma_{err,i}^2]} \times 100 \quad (3)$$

$$\Delta\sigma_{F_{var}}(\%) = \frac{1}{2} * \frac{\Delta\sigma_{NXV}^2}{\sqrt{\sigma_{NXV}^2}} \times 100, \quad (4)$$

where F_{var} is a linear statistic, which gives the same information as σ_{NXV}^2 , but in percentage terms. In order to compare the RMS and to account for the different exposure times, we split all light curves into 40ks segments, which is approximately a minimum-common-denominator segment for the long observations. Then we averaged the RMS results from the two or more segments available in longer (80–120 ks) observations and binned with ΔT of 1000 s. For the observations shorter than 40 ks, we did not estimate the RMS.

3. Main results

3.1. Spectral modelling

In this section we present the spectral analysis of NGC 1313 X-2. In order to obtain an adequate description of the continuum, ULX broadband X-ray spectra require several emission components. Among the several models tested, we adopted one similar model to that used in Walton et al. (2018c). All models also include neutral absorption, which was modelled with TBABS (Wilms et al. 2000). This absorption, which is due to an interstellar and circumstellar medium in the line of sight towards the source, is necessary to partially explain the low-energy spectral curvature. We adopted a lower limit equal to the Galactic value of $N_H = 7 \times 10^{20} \text{ cm}^{-2}$.

3.1.1. Baseline models

Our baseline model for the X-ray spectra of NGC 1313 X-2 consists of two thermal components, a cold disc blackbody (DISKBB) and a warmer DISKBB for the outer and the inner disc, respectively. It also consists of an exponential cutoff powerlaw component (CUTOFFPL) for the central accretion column that forms when the material flows down onto the magnetic poles. For the CUTOFFPL component, we set its spectral parameters to the average values seen from the pulsed emission of the following ULX pulsars currently known: $\Gamma = 0.59$ and $E_{cut} = 7.9$ keV (Brightman et al. 2016; Walton et al. 2018b,c,a).

In most spectra, there are notable residuals at ~ 1 keV, related to atomic emission and absorption associated with the likely

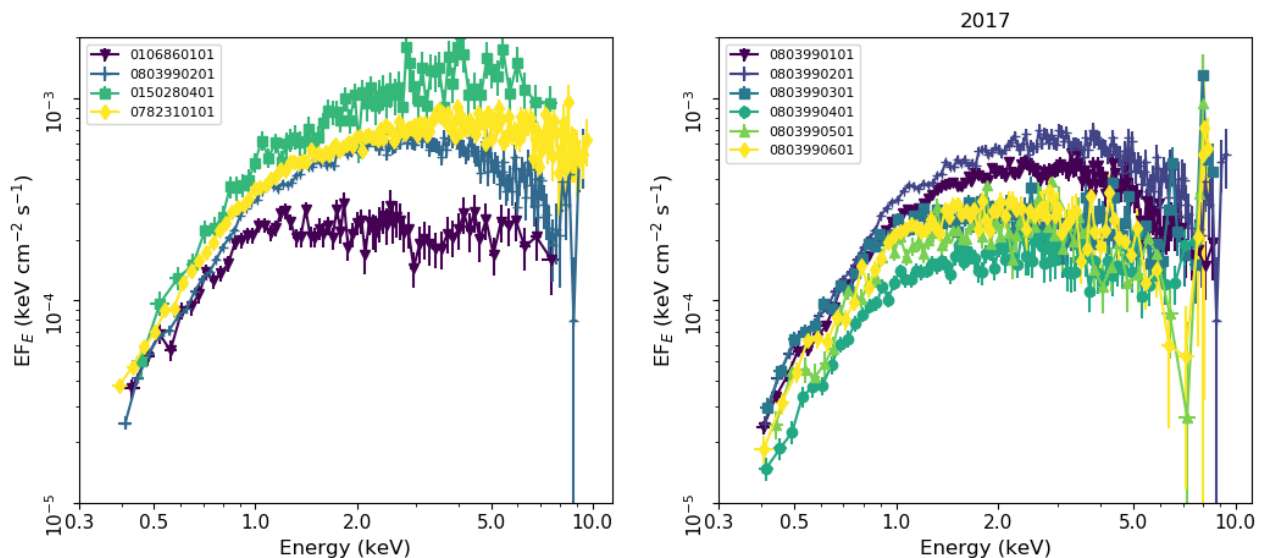


Fig. 2: Left panel: Comparison between four spectra, from low (Obs.ID:0106860101), to intermediate (Obs.ID:0803990201 and Obs.ID:0782310101), and to high flux (Obs.ID:0150280401). Right panel: *XMM-Newton*/EPIC-pn spectra of the recent observations (2017 campaign).

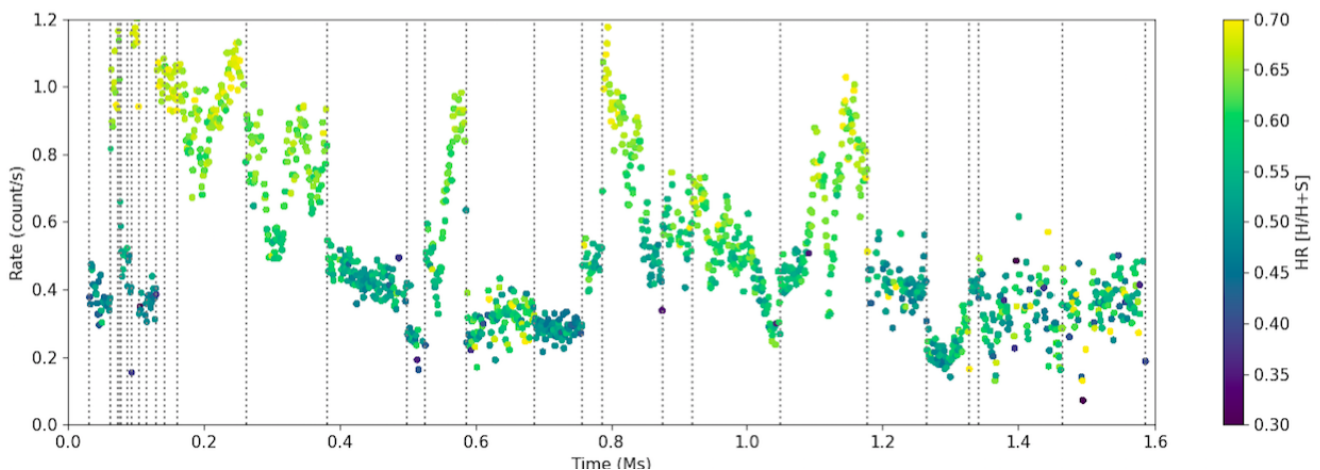


Fig. 3: 0.3–10 keV long-term EPIC/pn light curve of NGC 1313 X-2 colour-coded according to the HR for all the *XMM-Newton* observations, with time bins of 1000 s. The HR was computed using the light curves in the soft [0.3–1.2 keV] and in the hard [1.2–10 keV] X-ray energy bands. Observations occur at different epochs: we removed the gaps between observations with grey-dashed lines for visual purposes.

presence of an extreme outflow powered by wind (Pinto et al. 2016; Kosec et al. 2018a,b; Wang et al. 2019). Despite this, the overall shape of the X-ray spectra is well reproduced by our featureless continuum model. Indeed, as pointed by Pinto et al. (2020a) and Walton et al. (2020), the presence of the wind has no dramatic effects on the modelling of the spectral continuum and, therefore, we did not include any line emission or absorption components in our current fits. In addition, this would require the use of deep, on-axis, RGS spectra that are unavailable since the source is off-axis in most of the observations. This is valid for the optically thin ionised wind phase responsible for the spectral lines, but it might not hold in the case of further optically thick wind components.

The spectral fits with the best-fitting baseline double disc-blackbody and the exponential cutoff powerlaw models are presented in Appendix A. As we show in Table A.1, we obtained a column density between $N_H = (0.095\text{--}0.32) \times 10^{22} \text{ cm}^{-2}$, a cold temperature in the range from $0.20 < T_1 < 0.49 \text{ keV}$, and a warm temperature in the $0.69 < T_2 < 1.9 \text{ keV}$ range. The corresponding luminosities are $L_1 = (1\text{--}6) \times 10^{39} \text{ erg s}^{-1}$ and $L_2 = (2\text{--}8) \times 10^{39} \text{ erg s}^{-1}$. The goodness of the spectral fits is indicated by the χ^2 , which are satisfactory as shown in Table A.1 (the reduced χ^2 are in the range from 0.8–1.4).

3.1.2. Alternative models

We also tested several other models to describe the spectral shape of the spectrum of X-2. We show examples of our model fits for Obs.ID:0803990201 in Fig. 4 with corresponding best-fit parameters in Table 2.

Spectral modelling of ULXs using *XMM-Newton* data is well established with two-component models, which resemble multi-colour blackbody emission (e.g. Gladstone et al. 2009 and Stobart et al. 2006). In this context, the first attempt consists of a double disc-blackbody DISKBB+DISKBB, in which the first component describes the outer accretion flow and the possible optically thick wind and the second one takes both the inner flow and any other emission closer to the NS into account. As we expected (considering the lack of the hard cutoff powerlaw component), in comparison to the best-fitting model, the values of the temperatures are larger. The column densities, on the other hand, are similar (see Table B.1). We also tested the model with the column density fixed to $N_H = 1.94 \times 10^{21} \text{ cm}^{-2}$, obtained from the weighted average of the previous fits with free N_H , to evaluate the contribution of neutral absorption and systematic effects. However, we note that this assumption does not strongly influence the broadband continuum fits, so we preferred to keep N_H free to vary amongst the spectra.

The spectral fits with two thermal components are generally worse than the baseline three component model with the greatest discrepancy at the lowest flux, where the hard cutoff powerlaw component starts to be important ($\Delta\chi^2 = 41$ and 61 for Obs.ID 0405090101 and 0782310101, respectively, for 1 additional degree of freedom). Spectral parameters are reported in Appendix B (see Table B.1).

The second alternative model consists of replacing the double DISKBB continuum model with a single DISKBB modified by a SIMPL component. This empirical model of Comptonisation assumes that a fraction of the soft photons is scattered into a corona or a photosphere warmer than the disc. As shown in Table 2, although the parameters are physically acceptable, we found a worse fit with an increase of χ^2 ($\Delta\chi^2 = 140$) in observation 0803990201. Column densities, N_H , and cool temperature values are similar and follow the same behaviour as the baseline model with two DISKBBs plus a CUTOFFPL component.

Afterwards, we tried using a DISKBB+DISKPBB model, where DISKPBB is a multiple blackbody disc model characterised by the additional free parameter p (Mineshige et al. 1994). The p parameter defines the radial dependency of the temperature, following the law $T \propto R^{-p}$ ($p=0.75$ for a standard disc, $p<0.75$ for a profile affected by advection, and $p=0.5$ for a slim disc, see Abramowicz et al. 1988).

In this case, the temperatures obtained for the cool component are similar to parameters from the best-fit (in the DISKBB+DISKBB+CUTOFFPL baseline model); whereas for the hot component, the temperature is largely unconstrained in some observations. In general, the values for parameter p (e.g. $p=0.573 \pm 0.019$, for Obs.ID:0803990201) indicate a regime very close to the slim disc profile (the mean value for all spectral fits is $p_{\text{mean}} \sim 0.57$). The addition of the extra free parameter (p) provides spectral fits that are statistically halfway between the two DISKBB and three component models.

All the models show some residuals around 1 keV, as described in Section 3.1.1. They appear very similar and narrow (~ 0.1 keV) in all fits, indicating that they are independent from the particular model chosen and do not affect our results.

Table 2: Best-fit parameters for the models tested in this work for Obs.ID:0803990201.

TBABS*(DISKBB+DISKBB+CUTOFFPL)			
Model component	Parameter	Unit	
TBABS	N_H	$[10^{22} \text{ cm}^{-2}]$	0.28 ± 0.02
DISKBB	T_{in}	[keV]	0.25 ± 0.02
	norm		14^{+7}_{-5}
DISKBB	T_{in}	[keV]	1.13 ± 0.04
	norm		0.053 ± 0.007
CUTOFFPL	PhoIndex		0.59 (fixed)
	HighECut	[keV]	7.9 (fixed)
	norm	$[10^{-5}]$	$2.8^{+0.4}_{-0.5}$
χ^2/dof			314.91/259
TBABS*(DISKBB+DISKBB)			
Model component	Parameter	Unit	
TBABS	N_H	$[10^{22} \text{ cm}^{-2}]$	$0.242^{+0.014}_{-0.013}$
DISKBB	T_{in}	[keV]	0.32 ± 0.02
	norm		$4.3^{+1.7}_{-1.2}$
DISKBB	T_{in}	[keV]	$1.36^{+0.03}_{-0.02}$
	norm		0.028 ± 0.002
χ^2/dof			336.86/260
TBABS*(SIMPL*DISKBB)			
Model component	Parameter	Unit	
TBABS	N_H	$[10^{22} \text{ cm}^{-2}]$	$0.158^{+0.002}_{-0.004}$
SIMPL	Γ		$2.75^{+0.07}_{-0.02}$
DISKBB	T_{in}	[keV]	$0.56^{+0.01}_{-0.02}$
	norm		$0.62^{+0.09}_{-0.08}$
χ^2/dof			455.69/260
TBABS*(DISKBB+DISKPBB)			
Model component	Parameter	Unit	
TBABS	N_H	$[10^{22} \text{ cm}^{-2}]$	$0.32^{+0.03}_{-0.02}$
DISKBB	T_{in}	[keV]	0.21 ± 0.02
	norm		30^{+37}_{-15}
DISKPBB	T_{in}	[keV]	$1.57^{+0.07}_{-0.05}$
	p		0.57 ± 0.02
	norm		0.008 ± 0.002
χ^2/dof			321.32/259

3.2. Time variability

NGC 1313 X-2 shows high variability during the two decades of (non-contiguous) observations, as seen in the long-term light curve (see Fig. 3). Strong short-term (\sim hours) variability is also seen during some individual and long observations. We see that the source becomes harder when it is brighter, which is indicative of an increasingly brighter super-Eddington inner disc. This is because the hot disc is the dominant component in the 0.3–10 keV energy band.

The timing properties of X-2 were also probed using the fractional variability (see Section 2.4). The average values of F_{var} for several observations and the corresponding HR mean are presented in Table 3. We have reported only the values for the observations that have a common time baseline of exposure time (40 ks) for comparing the RMS estimated. The complete values

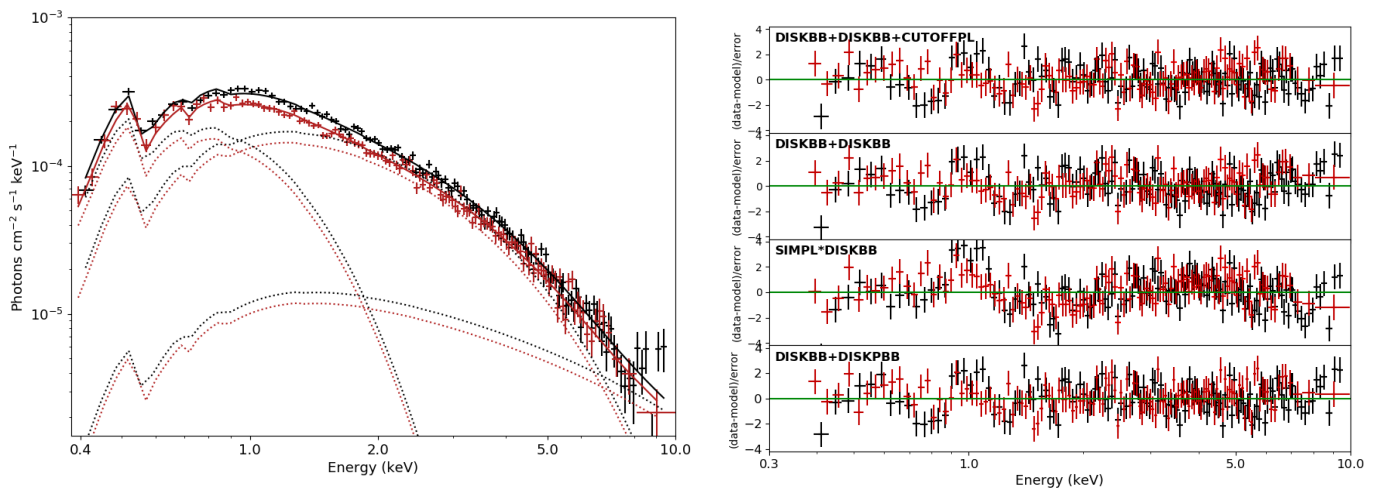


Fig. 4: Left panel: *XMM-Newton* unfolded spectrum of observation 0803990201 of NGC 1313 X-2. The black points are EPIC-pn and the red points show the stacked EPIC-MOS1/2 data. We overlapped the best-fit DISKBB+DISKBB+CUTOFFPL model (black and red, solid lines) and its single components (dashed lines). Right panel: Residuals from a selection of models listed in Table 2.

calculated for each segment are shown in Appendix C (see Table C.1). Also, in cases where the observed variance is less than the error associated with each bin, the excess variance value is negative. These values are excluded from our considerations.

As shown in Fig. 5, the variability of the source considerably increases in the observations with a higher flux, which is in agreement with the RMS-flux variability of accretion discs. Sutton et al. (2013) suggest that the increased flux variability observed at energies above 1 keV in ULXs with hard spectra can be attributed to the obscuration of the hard central emission when observed through the clumpy edge of the outflowing wind and from the photosphere of the super-Eddington disc.

Sathyaprakash et al. (2019) have found evidence of pulsations during observations Obs.ID:080399401 and Obs.ID:0803990601. This corresponds to the low-flux end of the new campaign, which suggests that the bright variable continuum is strongly affected by the inner accretion flow. In other words, at higher accretion rates the disc flux may significantly exceed the flux of the accretion column, thereby decreasing the pulse fraction. Walton et al. (2018c) also suggest this for the ensemble of ULXs observed by *NuSTAR*. In addition, this would imply a low-to-mild magnetic field ($B \lesssim 10^{12}$ G, see e.g. King & Lasota 2020), because the magnetospheric radius (R_m) is likely smaller than the spherisation radius (R_{sph}) for this object, given the presence of a bubble nebula (e.g. Pakull & Mirioni 2002) that is thought to be inflated by the disc wind.

4. Discussion

We have performed a detailed spectral analysis of the ultraluminous X-ray source NGC 1313 X-2, focussing on the *XMM-Newton* observations, with the aim of understanding the long-term behaviour of the spectral components. Given that the compact object is now known to be a NS, the accretion rate must be highly super-Eddington, and its spectral and temporal properties are expected to diverge from the case of sub-Eddington thin accretion discs.

As Vierdayanti et al. (2010) showed, the evolution of NGC 1313 X-2 appears similar to the archetypal ULX Holmberg IX X-1, characterised by strong spectral variability (see also Luangtip et al. 2016; Pintore et al. 2014; Walton et al. 2014). As

Table 3: Fractional variability measured using the average value of the EPIC-pn light curve segments for each observation with an exposure time of 40 ks and 1000 s bins.

Obs.ID	F_{var} mean (%)	HR mean
0405090101	6.06 ± 0.02	0.65 ± 0.03
0693850501	11.76 ± 0.07	0.62 ± 0.03
0693851201	0.748 ± 0.008	0.53 ± 0.04
0742590301	7.93 ± 0.07	0.61 ± 0.05
0742490101	3.26 ± 0.04	0.58 ± 0.07
0764770101	1.154 ± 0.002	0.49 ± 0.04
0782310101	12.17 ± 0.09	0.60 ± 0.07
0803990101	14.99 ± 0.04	0.60 ± 0.05
0803990201	12.93 ± 0.09	0.61 ± 0.05
0803990301	1.04 ± 0.04	0.52 ± 0.06
0803990401	1.91 ± 0.04	0.55 ± 0.06
0803990501	7.56 ± 0.16	0.55 ± 0.08
0803990601	4.79 ± 0.10	0.6 ± 0.1

reported by Walton et al. (2017), the spectra of Holmberg IX X-1 are well fit by two thermal blackbody components, which dominate the emission below 10 keV, plus a powerlaw tail which dominates above 10 keV.

As shown in Fig. 4, the spectrum is reasonably well described by a combination of two DISKBB plus a CUTOFFPL components. This model approximates super-Eddington accretion onto a NS, characterised by a standard outer disc, a thick inner disc region, and strong optically thick winds, which may contribute to the cooler component. In particular, the ~ 1 –10 keV band is mainly dominated by the hotter component, which describes the emission from the inner region, and the CUTOFFPL component representing the accretion column and the boundary layer near the NS. Instead, the emission from the outer disc or from the wind is responsible for the cooler blackbody component with a temperature around 0.3 keV. Wind is expected to be launched from the upper regions of the inner disc at accretion rates comparable to or higher than the Eddington limit. This scenario is supported by the presence of strong and narrow residuals around 1 keV that have been resolved in similar sources with the aid of high-resolution X-ray spectra (Pinto et al. 2016).

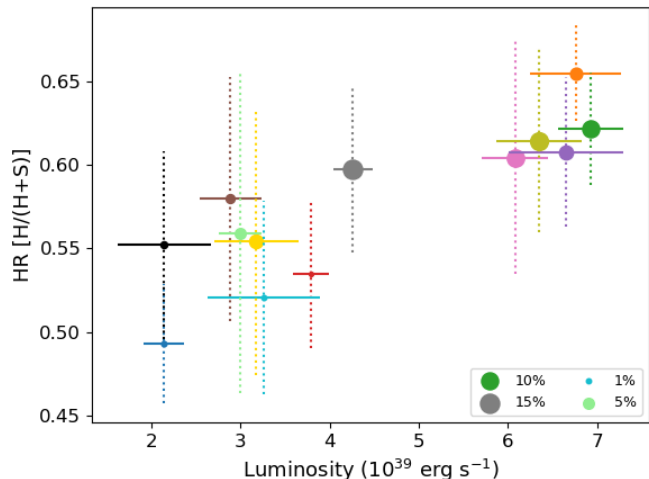


Fig. 5: Average HR (from the 1.2–10/0.3–10 keV energy bands) versus luminosity in linear space. The size of the markers correspond to the different values of the fractional variability (reported in Table 3).

The modelling of the spectra with high statistics shows that the column density, N_H , is broadly consistent with $\sim 2 \times 10^{21} \text{ cm}^{-2}$ (see Table A.1). Fixing the N_H (see Appendix D) does not strongly influence the broadband continuum fits, so we preferred to keep N_H free.

With the intention of improving the analysis, we tested several spectral models, as described in Section 3.1.2. When the accretion rate is high, the structure of the disc is expected to deviate considerably from the standard Shakura-Sunayev thin disc. For this reason, as reported by Bachetti et al. (2013), we replaced the hotter DISKBB with a DISKPBB component (we tested the DISKBB+DISKPBB model). Considering only the DISKPBB component, we have obtained similar results. Comparing the same observations analysed in Bachetti et al. (Obs.ID1:0693850501 and Obs.ID2:0693851201), we found the values of p to be consistent within 2σ (this work: $p_{ID1}=0.62\pm 0.03$ and $p_{ID2}=0.62^{+0.18}_{-0.07}$; Bachetti et al.: $p_{ID1}=0.58\pm 0.01$ and $p_{ID2}=0.500^{+0.006}_*$). We also found consistent temperatures (this work: $T_{in1}=1.52^{+0.06}_{-0.04}$ and $T_{in2}=1.15^{+0.06}_{-0.07}$; Bachetti et al.: $T_{in1}=1.56\pm 0.06$ and $T_{in2}=1.27\pm 0.05$). In general, for several observations, the p values are compatible with an accretion regime significantly affected by advection and they are sometimes close to the slim disk regime, which strongly argues in favour of super-Eddington accretion.

In the future we will use principal component analysis (PCA) to decompose the spectrum in a model-independent way (e.g. Pinto et al. 2020b). Moreover, we will search for winds with both PCA and physical models and then we will study how they vary with the spectral shape.

4.1. Luminosity-temperature plane

In this section we discuss the temporal behaviour of the two thermal components, investigating how they evolve in the luminosity-temperature plane. We calculated the unabsorbed luminosities (i.e. corrected for interstellar absorption by setting the column density $N_H=0$) for each of the thermal components individually, over the broad band from 0.001–10 keV, which pro-

vides their bolometric values. The comparison between the temperature and the luminosity of each component in the case of free column density is shown in Fig. 6. We show the L–T trends for both the cool (blue) and hot (orange) thermal components in the same figure because their separation in temperature is sufficiently high to avoid confusion.

It is very useful to compare the observed trends with the L–T $^\alpha$ relationships as expected from theoretical scenarios such as a sub-Eddington thin disc of Shakura-Sunayev ($L \propto T^4$ for constant emitting area, see Shakura & Sunyaev 1973) or an advection-dominated disc ($L \propto T^2$, see Watarai et al. 2000). These laws are shown as red-solid and green-dashed lines in Fig. 6, respectively.

The L–T trend observed for the hot disk-blackbody component is somewhere in between the two trends above. We do indeed obtain $\alpha_H = 3.0 \pm 0.35$ by fitting the L–T group of the hot component, which also argues in favour of super-Eddington accretion with a thicker disc.

The trend followed by the cool component is instead negative ($\alpha_C = -3.9 \pm 1.0$) and differs from the one expected from a sub-Eddington thin disc of Shakura-Sunayev ($L \propto T^4$) or an advection-dominated disc ($L \propto T^2$). Our results are in agreement with the interpretation of Qiu & Feng (2021), suggesting that the soft emission originates from the photosphere of the optically thick wind, driven by supercritical accretion. In this scenario, the measured blackbody luminosities of the PULXs are often higher than the Eddington limit of NSs, assuming spherical accretion (i.e. $L_{\text{EDD,NS}} = (1-3) \times 10^{38} \text{ erg s}^{-1}$). Moreover, we may expect an inversion of the L–T relationship at accretion rates much higher than the Eddington limit due to the expansion of the photosphere, which is marked by an increase in the size of the emitting region of the soft component and a decrease in temperature. This effect can be interpreted as the fact that the spherisation radius, where the strong winds start to be launched, would increase with the accretion rate, yielding lower temperatures at a higher luminosity (see, e.g. Poutanen et al. 2007.)

Although the nature of the compact object is unknown, the hotter disc component of NGC 1313 X-1 also exhibits a positive relation for the luminosity-temperature trend, consistent with the theoretical scenarios. Walton et al. (2020) did not seem to find a strong anti-correlation between L and T for the low-T component, but this might be due to the low number of spectra (seven) along with the more complex DISKBB+SIMPL*DISKPBB and DISKPBB+DISKBB+CUTOFFPL model.

In order to check the presence of the third component, we tested the L–T trends with the simpler DISKBB+DISKBB model. As can be seen from Fig. 7, the L–T trend observed for the hot disk-blackbody component shows a much more chaotic behaviour. Observations with better statistics (higher fluxes and longer durations) still sit somewhere in between the two theoretical cases outlined above, but there are considerable deviations for a cluster of points where the hotter component is characterised by high temperatures and low luminosities. Indeed, we obtain $\alpha_H = 2.8 \pm 0.6$ by fitting the L–T group of the hot component, which also argues in favour of super-Eddington accretion with a thicker disc. The trend followed by the cool component is instead much flatter ($\alpha_C = -0.13 \pm 0.36$) than the one expected from the theoretical scenarios. We conclude that the introduction of a third (CUTOFFPL) component significantly improves the spectral fits of some observations, which is confirmed by the detection of more regular trends in Fig. 6 and from their lower reduced χ^2 .

The presence of a correlation or anti-correlation between these points (luminosity and temperature for the hot and

cool components) for the baseline model was also verified by the computation of the correlation coefficients of Pearsons and Spearman (see Table 4). They were calculated using the PYTHON routines *scipy.stats.pearsonr* and *scipy.stats.spearmanr*. The result for the cooler component indicates a negative correlation and a positive correlation for the hotter component. The coefficients obtained are not very high because, as opposed to the least squares method, they do not take the error associated with the luminosity and temperature into account.

Table 4: Pearson and Spearman correlation coefficients calculated for the trends between luminosity and temperature for both the cool and the hot DISKBB components (assuming the baseline model, i.e. DISKBB+DISKBB+CUTOFFPL).

Parameters	Pearson	Spearman
$L_{hot}-T_{hot}$	0.69	0.69
$L_{cool}-T_{cool}$	-0.44	-0.47

The behaviour of the soft component has also been recently examined by [Gúrpide et al. \(2021\)](#). As they report, the significantly softer spectra of NGC 1313 X-2 can be explained by the scenario consistent with the wind structure responsible for highly anisotropic emission, given the wide HR variability the source spans. However, they do not report a clear correlation between the temperature and luminosity. Although their model is a double DISKBB model and thus is conceptually similar to ours, they adopted a different model for the high-energy component, using a SIMPL powerlaw continuum instead. As previously discussed, this may exacerbate parameter degeneracies when only soft X-ray data (i.e. <10 keV) are available, and this may explain the different conclusion found here. Moreover, for some observations they have used only pn spectra, resulting in a lower overall signal-to-noise ratio (S/N) and thus larger uncertainties. As we also suggest, they hypothesise that the observed residuals at soft energies around 1 keV can be produced by the presence of strong outflows. [Kajava & Poutanen \(2009\)](#) also studied the (L,T) relation of the soft component, although much less data were available at that time (i.e. prior to our new 2017 campaign). They found that, taken together, the soft component followed a trend $L_{soft} \propto T^{-3.5}$ for a sample of ULXs that included NGC 1313 X-2, although the behaviour of individual sources was not considered in detail. In addition, [Soria \(2007\)](#) showed an anti-correlation between the disc luminosity and temperature, supporting the non-standard outer disc. As [Soria \(2007\)](#) showed, if we assume that the boundary between the outer and inner disc scales as \dot{m} , the negative slope of the L–T relation depends on the T(R) function. For $T \sim R^{-0.5}$, it is expected that the $L \sim T^{-4}$, which is consistent with our result ($L \sim T^{-3.9}$). Therefore, we suggest that the outer disc is affected by the wind.

About 10% of the available data have also been analysed by [Pintore & Zampieri \(2012\)](#). They adopted a different model where the hot DISKBB is replaced with the much broader Comptonisation component, COMPTT. They also tied the temperature of the seed photons to that of the cool blackbody. For the broad X-ray spectra of ULXs, this has the effect of lowering the contribution in terms of flux from the cooler blackbody component. They reported a weak correlation between the luminosity of the soft component with the inner temperature, $L_{disc} \propto T_{disc}^{1.2 \pm 0.3}$.

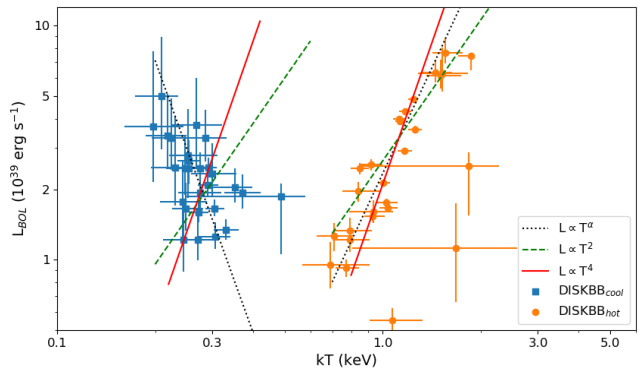


Fig. 6: 0.001–10 keV (i.e. bolometric) luminosity versus temperature for both the cool DISKBB (blue points) and hot DISKBB (orange points) components with free column density, N_H (model: DISKBB+DISKBB+CUTOFFPL).

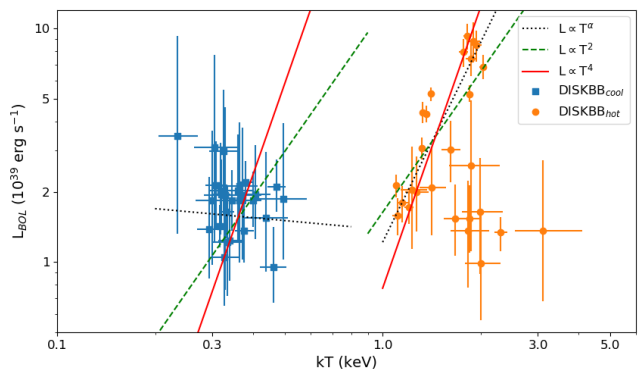


Fig. 7: 0.001–10 keV (i.e. bolometric) luminosity versus temperature for both the cool DISKBB (blue points) and hot DISKBB (orange points) components with free column density, N_H (model: DISKBB+DISKBB).

4.2. Radius-luminosity relation

In order to test the consistency with the luminosity-temperature trends, we also estimated the mean inner radii for the DISKBB component for each of the two groups, using the normalisation factor with the formula $R_{in} = \sqrt{(norm * D_{10}^2) / \cos i}$, where D_{10} is the distance to the source in units of 10 kpc and i is the inclination of the disc. The mean inner radii are $R_{in,1} \sim 1722 (\cos i)^{-1/2}$ km and $R_{in,2} \sim 146 (\cos i)^{-1/2}$ km (where subscripts 1 and 2 refer to the lower and higher temperature tracks, respectively), which correspond to $\sim 414 R_S$ and $\sim 35 R_S$ (where $R_S = 2GM/c^2$ is the Schwarzschild radius, assuming $M = 1.4 M_\odot$).

Using the relation $L = A\sigma T^4$, we can also determine the emitting areas for each DISKBB component, as shown in Fig. 8. We note that, for the hot component, the size of the emitting area of the accretion disc is broadly constant (in units of $R_{NS} = 10$ km, $\Delta R \sim 57 R_{NS}$) for several observations. Instead, the emitting area for the cool component varies from $R_{min} \sim 180 R_{NS}$ to $R_{max} \sim 1600 R_{NS}$. This would agree with the expectations from a local increase in the accretion rate ([Poutanen et al. 2007](#)).

Using the formalism outlined in [King & Lasota \(2020\)](#) and assuming $20 < \dot{m} < 25$ (which is reasonable for the observed luminosity), we can also estimate the spherisation radius $R_{sph} \sim 70-87 R_S$. We found that the inner radius for the cool component is larger than the spherisation radius, that is $R_{in,1} > R_{sph}$,

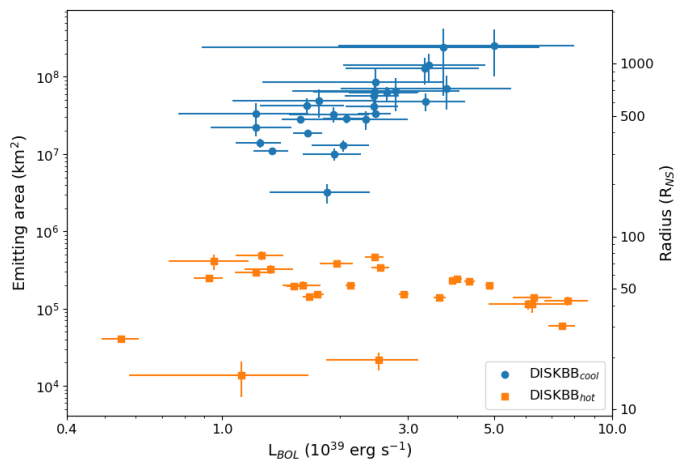


Fig. 8: Left Y-axis: Emitting area versus luminosity for both the cool and hot DISKBB components (blue and orange points, respectively). Right Y-axis: Radius, in units of typical NS radius of 10 km, versus luminosity for both the cool and hot DISKBB components (blue and orange points, respectively).

which suggests that the cool component takes both the emission from the cool disc and the contribution from the wind in account. The inner radius of the hot DISKBB is instead smaller than the spherisation radius ($R_{in,2} < R_{sph}$), indicating that this component is likely reproducing the super-Eddington inner accretion flow within R_{sph} .

Our approach has made use of phenomenological models in order to describe the long-term spectral evolution of the source. Future work will benefit from adopting physically motivated models which account for the thick nature of super-Eddington discs and Compton scattering through the disc atmosphere.

5. Conclusions

In this paper we have presented the analysis of the X-ray emission spectrum of NGC 1313 X-2, a pulsating ultraluminous X-ray source, using all the available observations performed by *XMM-Newton* between 2000 and 2017. With the aim of characterising the spectral shape and its long-term variability, we have tested various spectral models for all observations. Since pulsations have been detected, we know that the compact object is a NS. In order to reach high luminosities (up to 10^{40} erg s^{-1} in some observations), the compact object must be in a super-Eddington accretion regime.

The spectral model that provides the best description of the *XMM-Newton*/EPIC data consists of two multi-colour disk blackbody components plus an exponential cutoff powerlaw, as in [Walton et al. \(2018c\)](#). Similar to previous works, we find that the hotter of the two thermal components dominates the 1–10 keV band, and the cooler one is more relevant in the energy band below 1 keV. Furthermore, we found that the inner radius of the hot component is smaller than the spherisation radius, while the characteristic radii associated with the cooler component are all larger than the spherisation radius. In the framework of super Eddington accretion, this is strong evidence that the hotter component describes the dominant emission from the innermost region of the disc. Instead, the cooler component accounts for the emission from a larger region of the disc, outside the spherisation radius and the characteristic wind launching radius. Finally,

we argued that the cutoff powerlaw component comes from the accretion columns onto the NS.

Most spectra show narrow residuals around ~ 1 keV, which are likely associated with atomic emission and absorption lines produced by powerful outflows, as they are qualitatively similar to those seen in other ULXs that have been resolved and identified with the aid of dedicated high-resolution observations (see e.g. [Pinto et al. 2020b](#)). The luminosity and the temperature of each emission component evolves along L–T trends that deviate from those expected for some typical regimes such as the sub-Eddington thin disc of Shakura-Sunayev ($L \propto T^4$, for constant emitting area) or the advection-dominated disc ($L \propto T^2$). In particular, we obtain power indexes of $\alpha_H = 3.0 \pm 0.35$ and $\alpha_C = -3.9 \pm 1.0$ for the hotter and the cooler components, respectively. This implies a super-Eddington accretion regime and suggests a geometry closer to the funnel than a thin disk for the inner regions due to intense radiation pressure. Optically thick winds are also likely responsible for the scatter seen in Fig. 6.

This behaviour is qualitatively similar to the broadband spectral evolution seen in NGC 1313 X-1 and Holmberg IX X-1. The similar spectral evolution between these sources, where the flux above 1 keV increases significantly at higher luminosity, may indicate a common structure and evolution among archetypal ULXs.

Acknowledgements. The authors would like to thank the anonymous referee, who provided useful suggestions for improving the final manuscript. This work is based on observations obtained with *XMM-Newton*, an ESA science mission funded by ESA Member States and USA (NASA). DJW acknowledges support from STFC in the form of an Ernest Rutherford fellowship (ST/N004027/1). TPR gratefully acknowledges support from the Science and Technology Facilities Council (STFC) as part of the consolidated grant award ST/000244/1

References

- Abbott, B. P., Abbott, R., Abbott, T. D., et al. 2016a, *Phys. Rev. X*, 6, 041015
 Abbott, B. P., Abbott, R., Abbott, T. D., et al. 2016b, *Phys. Rev. Lett.*, 116, 061102
 Abbott, B. P., Abbott, R., Abbott, T. D., et al. 2019, *Physical Review X*, 9, 031040
 Abramowicz, M. A., Czerny, B., Lasota, J. P., & Szuszkiewicz, E. 1988, *ApJ*, 332, 646
 Arnaud, K. A. 1996, in *Astronomical Society of the Pacific Conference Series*, Vol. 101, *Astronomical Data Analysis Software and Systems V*, ed. G. H. Jacoby & J. Barnes, 17
 Bachetti, M., Harrison, F. A., Walton, D. J., et al. 2014, *Nature*, 514, 202
 Bachetti, M., Rana, V., Walton, D. J., et al. 2013, *ApJ*, 778, 163
 Brightman, M., Harrison, F., Walton, D. J., et al. 2016, *ApJ*, 816, 60
 Carpano, S., Haberl, F., Maitra, C., & Vasilopoulos, G. 2018, *MNRAS*, 476, L45
 Colbert, E. J. M. & Mushotzky, R. F. 1999, *ApJ*, 519, 89
 Farrell, S. A., Webb, N. A., Barret, D., Godet, O., & Rodrigues, J. M. 2009, *Nature*, 460, 73
 Fürst, F., Walton, D. J., Harrison, F. A., et al. 2016, *ApJ*, 831, L14
 Gladstone, J. C., Roberts, T. P., & Done, C. 2009, *MNRAS*, 397, 1836
 Gúrpide, A., Godet, O., Koliopoulos, F., Webb, N., & Olive, J.-F. 2021, *arXiv e-prints*, arXiv:2102.11159
 Heida, M., Lau, R. M., Davies, B., et al. 2019, *ApJ*, 883, L34
 Israel, G. L., Belfiore, A., Stella, L., et al. 2017a, *Science*, 355, 817
 Israel, G. L., Papitto, A., Esposito, P., et al. 2017b, *MNRAS*, 466, L48
 Kaaret, P., Feng, H., & Roberts, T. P. 2017, *ARA&A*, 55, 303
 Kajava, J. J. E. & Poutanen, J. 2009, *MNRAS*, 398, 1450
 King, A. & Lasota, J.-P. 2020, *MNRAS*, 494, 3611
 King, A., Lasota, J.-P., & Kluźniak, W. 2017, *MNRAS*, 468, L59
 King, A. R., Davies, M. B., Ward, M. J., Fabbiano, G., & Elvis, M. 2001, *ApJ*, 552, L109
 Koliopoulos, F., Vasilopoulos, G., Godet, O., et al. 2017, *A&A*, 608, A47
 Kosec, P., Pinto, C., Fabian, A. C., & Walton, D. J. 2018a, *MNRAS*, 473, 5680
 Kosec, P., Pinto, C., Walton, D. J., et al. 2018b, *MNRAS*, 479, 3978
 Kovelakos, K., Zezas, A., Andrews, J. J., et al. 2020, *MNRAS*, 498, 4790
 Luangtip, W., Roberts, T. P., & Done, C. 2016, *MNRAS*, 460, 4417
 Lumb, D. H., Warwick, R. S., Page, M., & De Luca, A. 2002, *A&A*, 389, 93

- Mendez, B., Davis, M., Newman, J., et al. 2002, in American Astronomical Society Meeting Abstracts, Vol. 201, American Astronomical Society Meeting Abstracts, 23.06
- Middleton, M. J. & King, A. 2016, MNRAS, 462, L71
- Middleton, M. J., Walton, D. J., Fabian, A., et al. 2015, MNRAS, 454, 3134
- Middleton, M. J., Walton, D. J., Roberts, T. P., & Heil, L. 2014, MNRAS, 438, L51
- Mineshige, S., Hirano, A., Kitamoto, S., Yamada, T. T., & Fukue, J. 1994, ApJ, 426, 308
- Nandra, K., George, I. M., Mushotzky, R. F., Turner, T. J., & Yaqoob, T. 1997, ApJ, 476, 70
- Pakull, M. W. & Mirioni, L. 2002, arXiv e-prints, astro
- Pinto, C., Alston, W., Soria, R., et al. 2017, MNRAS, 468, 2865
- Pinto, C., Mehdipour, M., Walton, D. J., et al. 2020a, MNRAS, 491, 5702
- Pinto, C., Middleton, M. J., & Fabian, A. C. 2016, Nature, 533, 64
- Pinto, C., Walton, D. J., Kara, E., et al. 2020b, MNRAS, 492, 4646
- Pintore, F. & Zampieri, L. 2012, MNRAS, 420, 1107
- Pintore, F., Zampieri, L., Stella, L., et al. 2017, ApJ, 836, 113
- Pintore, F., Zampieri, L., Wolter, A., & Belloni, T. 2014, MNRAS, 439, 3461
- Poutanen, J., Lipunova, G., Fabrika, S., Butkevich, A. G., & Abolmasov, P. 2007, Monthly Notices of the Royal Astronomical Society, 377, 1187
- Qing, G., Wang, W., Liu, J.-F., & Yoachim, P. 2015, ApJ, 799, 19
- Qiu, Y. & Feng, H. 2021, ApJ, 906, 36
- Rodríguez Castillo, G. A., Israel, G. L., Belfiore, A., et al. 2020, ApJ, 895, 60
- Sathyaprakash, R., Roberts, T. P., Walton, D. J., et al. 2019, MNRAS, L104
- Shakura, N. I. & Sunyaev, R. A. 1973, A&A, 500, 33
- Soria, R. 2007, Ap&SS, 311, 213
- Stobart, A. M., Roberts, T. P., & Wilms, J. 2006, MNRAS, 368, 397
- Strüder, L., Briel, U., Dennerl, K., et al. 2001, A&A, 365, L18
- Sutton, A. D., Roberts, T. P., & Middleton, M. J. 2013, MNRAS, 435, 1758
- Swartz, D. A., Tennant, A. F., & Soria, R. 2009, ApJ, 703, 159
- Tully, R. B., Courtois, H. M., & Sorce, J. G. 2016, AJ, 152, 50
- Turner, M. J. L., Abbey, A., Arnaud, M., et al. 2001, A&A, 365, L27
- Vaughan, S., Edelson, R., Warwick, R. S., & Uttley, P. 2003, MNRAS, 345, 1271
- Vierdayanti, K., Done, C., Roberts, T. P., & Mineshige, S. 2010, MNRAS, 403, 1206
- Walton, D. J., Bachetti, M., Fürst, F., et al. 2018a, ApJ, 857, L3
- Walton, D. J., Fürst, F., Harrison, F. A., et al. 2017, ApJ, 839, 105
- Walton, D. J., Fürst, F., Harrison, F. A., et al. 2018b, MNRAS, 473, 4360
- Walton, D. J., Fürst, F., Heida, M., et al. 2018c, ApJ, 856, 128
- Walton, D. J., Harrison, F. A., Grefenstette, B. W., et al. 2014, ApJ, 793, 21
- Walton, D. J., Middleton, M. J., Pinto, C., et al. 2016, ApJ, 826, L26
- Walton, D. J., Pinto, C., Nowak, M., et al. 2020, MNRAS, 494, 6012
- Wang, C., Soria, R., & Wang, J. 2019, ApJ, 883, 44
- Watarai, K.-y., Fukue, J., Takeuchi, M., & Mineshige, S. 2000, PASJ, 52, 133
- Wiktorowicz, G., Lasota, J.-P., Middleton, M., & Belczynski, K. 2019, ApJ, 875, 53
- Wilms, J., Allen, A., & McCray, R. 2000, ApJ, 542, 914
- Zampieri, L. & Roberts, T. P. 2009, MNRAS, 400, 677

Appendix A: Table best-fit parameters

Table [A.1](#) reports the results of the spectral fits with the DISKBB+DISKBB+CUTOFFPL model for all *XMM-Newton* observations of X-2.

Table A.1: Best fitting spectral parameters of NGC1313 X-2 in different observations with the absorbed DISKBB+DISKBB+CUTOFFPL model.

ObsID	N_H (10^{22} cm $^{-2}$)	T_1 (keV)	norm ₁	L_1 ^(*) (10^{39} erg/s)	T_2 (keV)	norm ₂	L_2 ^(*) (10^{39} erg/s)	norm ₃ (10^{-5})	χ^2 /dof
0106860101	0.286 ^{+0.06} _{-0.04}	0.219 ± 0.03	30 ⁺⁵⁷ ₋₁₆	3.4 ^{+1.7} _{-1.0}	0.71 ^{+0.10} _{-0.08}	0.11 ^{+0.08} _{-0.05}	1.26 ^{+0.18} _{-0.17}	4.0 ± 0.3	137.31/144
0150280101	0.10 ^{+0.05} _{-0.03}	0.5 ^{+1.8} _{-0.5}	0.13 ⁺⁹²³ _{-0.13}	5.75 ⁺²⁴ ₋₅	1.4 ⁺⁸ _{-1.3}	0.03 ^{+0.03} _{-0.01}	5.2 ^{+1.1} _{-1.0}	1.0 ^{+6.0} _{-1.0}	64.91/63
0150280301	0.19 ± 0.02	0.37 ± 0.05	2.3 ^{+1.4} _{-0.9}	1.9 ^{+0.4} _{-0.3}	1.871 ^{+0.04} _{-0.16}	0.014 ^{+0.004} _{-0.002}	7.46 ^{+0.16} _{-1.1}	0.02 ⁺³ _{-0.02}	161.42/191
0150280401	0.27 ^{+0.05} _{-0.04}	0.27 ^{+0.05} _{-0.04}	15 ⁺³³ ₋₁₀	3.8 ⁺² _{-1.3}	1.5 ^{+0.3} _{-0.2}	0.027 ^{+0.017} _{-0.010}	6.3 ^{+1.8} _{-1.1}	9 ⁺⁵ ₋₇	165.28/158
0150280501	0.13 ^{+0.03} _{-0.02}	0.49 ^{+0.02} _{-0.06}	0.005 ^{+0.10} _{-0.003}	1.86 ^{+0.3} _{-0.8}	1.8 ^{+0.4} _{-0.2}	0.73 ⁺⁴¹ ₋₃₅	2.5 ^{+0.4} _{-0.4}	0.01 ^{+6.0} _{-0.01}	86.77/87
0150280601	0.26 ^{+0.06} _{-0.05}	0.23 ^{+0.06} _{-0.04}	21 ⁺⁴⁸ ₋₁₅	2.47 ^{+1.8} _{-0.8}	0.84 ^{+0.14} _{-0.09}	0.09 ^{+0.06} _{-0.04}	1.97 ^{+0.18} _{-0.2}	3.1 ^{+0.6} _{-0.7}	151.03/122
0150281101	0.32 ^{+0.08} _{-0.05}	0.2 ^{+0.05} _{-0.04}	0.05 ^{+0.05} _{-0.018}	5 ⁺⁴ ₋₂	0.94 ^{+0.14} _{-0.15}	50 ⁺¹⁶⁶ ₋₂₉	1.6 ± 0.18	3.0 ^{+0.3} _{-1.0}	62.86/82
0205230301	0.27 ± 0.03	0.29 ^{+0.05} _{-0.03}	1.56 ^{+0.11} _{-0.14}	3.32 ^{+1.1} _{-0.7}	0.029 ^{+0.009} _{-0.008}	11 ⁺²⁹ ₋₅	7.7 ^{+1.2} _{-0.8}	7 ⁺³ ₋₅	212.25/210
0205230401	0.31 ^{+0.08} _{-0.07}	0.20 ^{+0.05} _{-0.04}	0.09 ^{+0.17} _{-0.07}	3.7 ⁺⁴ _{-1.6}	0.69 ^{+0.2} _{-0.12}	55 ⁺⁵⁸ ₋₄₁	1.0 ± 0.2	3.5 ^{+0.5} _{-0.6}	82.88/90
0205230501	0.29 ^{+0.05} _{-0.04}	0.22 ± 0.03	0.07 ^{+0.07} _{-0.03}	3.3 ^{+1.6} _{-0.9}	0.8 ^{+0.2} _{-0.09}	28 ⁺⁴⁴ ₋₁₅	1.22 ± 0.14	3.2 ± 0.4	130.98/128
0205230601	0.26 ± 0.05	0.25 ^{+0.06} _{-0.03}	15 ⁺²⁴ ₋₁₁	2.8 ^{+1.6} _{-0.8}	1.51 ^{+0.2} _{-0.15}	0.026 ^{+0.010} _{-0.009}	6.1 ^{+1.1} _{-0.7}	9 ⁺³ ₋₄	178.94/213
0301860101	0.25 ± 0.03	0.30 ^{+0.04} _{-0.06}	6 ⁺⁹ ₋₄	2.3 ^{+0.8} _{-0.5}	1.45 ^{+0.15} _{-0.14}	0.03 ^{+0.012} _{-0.009}	6.3 ^{+0.7} _{-0.6}	7 ⁺⁴ ₋₄	210.74/218
0405090101	0.240 ^{+0.016} _{-0.015}	0.275 ^{+0.02} _{-0.019}	9 ⁺³ ₋₃	2.3 ^{+0.8} _{-0.5}	1.17 ^{+0.06} _{-0.05}	0.051 ± 0.008	4.31 ^{+0.14} _{-0.11}	12.2 ± 0.7	350.97/300
0693850501	0.235 ^{+0.015} _{-0.014}	0.290 ^{+0.02} _{-0.019}	0.046 ^{+0.006} _{-0.005}	2.1 ^{+0.3} _{-0.2}	1.24 ± 0.04	6 ⁺³ ₋₂	4.85 ^{+0.11} _{-0.10}	2.4 ^{+0.5} _{-0.5}	297.79/284
0693851201	0.218 ± 0.013	0.31 ± 0.02	0.046 ^{+0.009} _{-0.008}	1.66 ^{+0.16} _{-0.13}	1.01 ^{+0.05} _{-0.04}	4.3 ^{+1.7} _{-1.2}	2.1 ± 0.06	0.5 ± 0.2	265.81/235
0722650101	0.19 ^{+0.05} _{-0.03}	0.31 ^{+0.05} _{-0.08}	3.0 ⁺¹³ _{-1.5}	1.25 ^{+0.3} _{-0.4}	1.0 ⁺⁵ _{-0.4}	0.005 ⁺² _{-0.005}	0.17 ^{+1.3} _{-2e+12}	4.2 ^{+0.3} _{-4.2}	63.42/72
0742590301	0.28 ^{+0.03} _{-0.02}	0.3 ± 0.02	0.055 ^{+0.010} _{-0.009}	2.6 ^{+0.6} _{-0.4}	1.13 ± 0.05	15 ⁺¹⁰ ₋₆	4.01 ± 0.12	2.5 ± 0.6	281.44/231
0742490101	0.25 ± 0.03	0.3 ^{+0.04} _{-0.03}	5 ⁺⁵ ₋₃	1.2 ^{+0.3} _{-0.2}	1.04 ^{+0.08} _{-0.06}	0.032 ^{+0.009} _{-0.008}	1.67 ± 0.06	0.8 ± 0.3	226.31/197
0764770101	0.214 ^{+0.018} _{-0.017}	0.272 ^{+0.02} _{-0.018}	7 ⁺² ₋₂	1.59 ^{+0.19} _{-0.14}	1.07 ^{+0.3} _{-0.16}	0.009 ^{+0.005} _{-0.005}	0.55 ^{+0.07} _{-0.03}	3.2 ^{+0.3} _{-0.4}	173.59/227
0764770401	0.24 ^{+0.05} _{-0.04}	0.24 ^{+0.05} _{-0.04}	12 ⁺²³ ₋₇	1.8 ^{+0.9} _{-0.5}	0.85 ^{+0.06} _{-0.05}	0.11 ± 0.03	2.46 ^{+0.13} _{-0.11}	1.7 ± 0.4	178.34/167
0782310101	0.235 ^{+0.013} _{-0.012}	0.292 ^{+0.018} _{-0.016}	0.032 ^{+0.006} _{-0.005}	2.5 ^{+0.3} _{-0.3}	1.26 ± 0.06	7 ⁺³ ₋₂	3.61 ^{+0.13} _{-0.11}	7.3 ^{+0.6} _{-0.7}	339.58/290
0794580601	0.25 ^{+0.05} _{-0.04}	0.25 ± 0.03	0.08 ^{+0.005} _{-0.02}	2.5 ^{+0.9} _{-0.6}	0.92 ± 0.07	15 ⁺²¹ ₋₈	2.55 ^{+0.13} _{-0.14}	5.0 ± 0.6	193.82/187
0803990101	0.216 ^{+0.014} _{-0.013}	0.33 ± 0.03	2.5 ^{+1.3} _{-0.8}	11.34 ^{+0.15} _{-0.12}	1.17 ^{+0.06} _{-0.05}	0.035 ^{+0.007} _{-0.006}	2.92 ± 0.08	1.3 ± 0.4	229.80/249
0803990201	0.281 ^{+0.019} _{-0.018}	0.254 ^{+0.019} _{-0.016}	0.053 ± 0.007	2.5 ^{+0.4} _{-0.3}	1.13 ± 0.04	14 ⁺⁷ ₋₅	3.90 ± 0.09	2.8 ± 0.4	314.91/259
0803990301	0.225 ^{+0.018} _{-0.014}	0.28 ^{+0.05} _{-0.04}	7 ⁺⁹ ₋₄	1.9 ^{+0.6} _{-0.3}	0.80 ^{+0.13} _{-0.09}	0.07 ^{+0.06} _{-0.04}	1.33 ^{+0.19} _{-0.19}	3.4 ± 0.3	229.31/182
0803990401	0.27 ^{+0.05} _{-0.04}	0.24 ^{+0.04} _{-0.03}	0.056 ^{+0.03} _{-0.008}	1.2 ^{+0.6} _{-0.3}	0.8 ^{+0.07} _{-0.06}	7 ⁺¹¹ ₋₄	0.93 ^{+0.08} _{-0.08}	2.3 ± 0.2	152.54/175
0803990701	0.20 ^{+0.04} _{-0.03}	0.35 ^{+0.03} _{-0.03}	0.004 ^{+0.008} _{-0.001}	2.0 ^{+0.4} _{-0.3}	1.7 ± 0.9	3.0 ⁺⁶ _{-1.3}	1.1 ^{+0.6} _{-0.5}	1.5 ⁺³ _{-0.4}	95.17/70
0803990501	0.27 ^{+0.03} _{-0.04}	0.25 ^{+0.03} _{-0.02}	10 ⁺⁸ ₋₅	1.7 ^{+0.3} _{-0.3}	0.93 ^{+0.08} _{-0.08}	0.045 ± 0.013	1.53 ± 0.07	0.9 ^{+0.3} _{-0.4}	180.76/184
0803990601	0.210 ^{+0.02} _{-0.018}	0.31 ± 0.03	3.18 ⁺³ _{-1.2}	1.25 ^{+0.19} _{-0.14}	1.03 ^{+0.08} _{-0.08}	0.035 ^{+0.013} _{-0.010}	1.75 ^{+0.07} _{-0.08}	0.7 ± 0.4	215.32/200

Notes: Parameter uncertainties were estimated at 68%. ^(*)Luminosity values (in units of 10^{39} erg/s) are quoted for the unabsorbed model integrated over 0.3–10 keV.

Appendix B: Table DISKBB+DISKBB parameters

Table B.1 reports the results of the spectral fits with the DISKBB+DISKBB model for all *XMM-Newton* observations of X-2. Fig. B.1 shows the associated residuals for the best-fit model.

Table B.1: Best fitting spectral parameters of NGC1313 X-2 in different observations obtained with the absorbed DISKBB+DISKBB model.

ObsID	N_H (10^{22} cm^{-2})	T_1 (keV)	norm_1	T_2 (keV)	norm_2	χ^2/dof
0106860101	$0.199^{+0.018}_{-0.016}$	$0.34^{+0.02}_{-0.02}$	$3.2^{+1.4}_{-0.9}$	$1.82^{+0.17}_{-0.14}$	$0.0031^{+0.0012}_{-0.0009}$	149.14/145
0150280101	$0.089^{+0.2}_{-0.03}$	$0.7^{+6}_{-0.8}$	$0.05^{+101}_{-0.05}$	$1.5^{+1.5}_{-0.2}$	$0.023^{+0.018}_{-0.02}$	64.92/64
0150280301	0.19 ± 0.02	0.371 ± 0.05	$2.3^{+2}_{-1.1}$	$1.87^{+0.08}_{-0.07}$	0.014 ± 0.002	161.42/192
0150280401	0.24 ± 0.04	$0.3^{+0.06}_{-0.04}$	8^{+11}_{-5}	$1.90^{+0.10}_{-0.09}$	0.016 ± 0.003	166.83/159
0150280501	0.50 ± 0.09	$0.7^{+0.8}_{-0.3}$	$1.9^{+0.4}_{-0.3}$	$0.13^{+0.03}_{-0.02}$	$0.005^{+0.004}_{-0.003}$	86.77/88
0150280601	$0.19^{+0.03}_{-0.02}$	0.363 ± 0.05	$2.4^{+2}_{-1.1}$	$1.42^{+0.15}_{-0.12}$	$0.012^{+0.006}_{-0.004}$	157.38/123
0150281101	0.29 ± 0.06	$0.23^{+0.04}_{-0.03}$	26^{+43}_{-16}	$1.27^{+0.12}_{-0.10}$	$0.017^{+0.007}_{-0.006}$	66.69/83
0205230301	$0.25^{+0.03}_{-0.02}$	$0.33^{+0.04}_{-0.03}$	6^{+5}_{-3}	$1.82^{+0.06}_{-0.05}$	$0.020^{+0.003}_{-0.002}$	213.96/211
0205230401	$0.20^{+0.04}_{-0.03}$	$0.30^{+0.04}_{-0.03}$	5^{+5}_{-3}	$1.8^{+0.3}_{-0.2}$	$0.0028^{+0.0018}_{-0.0012}$	88.09/91
0205230501	0.213 ± 0.02	0.32 ± 0.03	$4.4^{+3}_{-1.6}$	$1.67^{+0.16}_{-0.13}$	$0.0045^{+0.0018}_{-0.0014}$	142.92/129
0205230601	$0.21^{+0.04}_{-0.03}$	$0.33^{+0.07}_{-0.05}$	4^{+5}_{-2}	$1.94^{+0.08}_{-0.07}$	0.014 ± 0.002	181.97/214
0301860101	0.225 ± 0.02	$0.36^{+0.05}_{-0.04}$	$2.7^{+2}_{-1.3}$	1.77 ± 0.06	0.019 ± 0.003	213.29/219
0405090101	$0.182^{+0.008}_{-0.007}$	0.47 ± 0.03	$0.9^{+0.3}_{-0.2}$	2.03 ± 0.06	$0.0095^{+0.0012}_{-0.0011}$	411.82/301
0693850501	0.213 ± 0.010	0.35 ± 0.02	$2.8^{+1.0}_{-0.7}$	1.41 ± 0.02	0.030 ± 0.002	310.06/285
0693851201	$0.208^{+0.011}_{-0.010}$	$0.331^{+0.019}_{-0.017}$	$3.0^{+0.9}_{-0.7}$	$1.10^{+0.03}_{-0.02}$	0.033 ± 0.004	269.55/236
0722650101	0.175 ± 0.03	$0.333^{+0.04}_{-0.03}$	$2.3^{+1.7}_{-1.0}$	$3.1^{+1.0}_{-0.6}$	$0.0004^{+0.0004}_{-0.0002}$	63.79/73
0742590301	$0.245^{+0.018}_{-0.017}$	$0.31^{+0.03}_{-0.02}$	$5.5^{+3}_{-1.9}$	1.33 ± 0.03	$0.0316^{+0.0033}_{-0.0032}$	292.76/232
0742490101	$0.218^{+0.02}_{-0.018}$	0.33 ± 0.03	$2.1^{+1.4}_{-0.8}$	1.21 ± 0.04	0.018 ± 0.003	230.70/198
0764770101	0.186 ± 0.011	0.316 ± 0.012	$3.2^{+0.7}_{-0.6}$	$2.30^{+0.11}_{-0.10}$	0.0012 ± 0.0002	182.24/228
0764770401	$0.167^{+0.02}_{-0.017}$	0.44 ± 0.07	$0.9^{+0.8}_{-0.4}$	$1.23^{+0.14}_{-0.09}$	$0.020^{+0.011}_{-0.009}$	186.74/168
0782310101	0.201 ± 0.008	$0.380^{+0.018}_{-0.017}$	$2.3^{+0.6}_{-0.4}$	1.85 ± 0.04	$0.0103^{+0.0009}_{-0.0008}$	380.93/291
0794580601	$0.175^{+0.018}_{-0.016}$	$0.41^{+0.05}_{-0.04}$	$1.6^{+1.0}_{-0.6}$	$1.62^{+0.12}_{-0.10}$	0.010 ± 0.003	213.02/188
0803990101	$0.204^{+0.011}_{-0.010}$	0.38 ± 0.03	$1.5^{+0.6}_{-0.4}$	1.32 ± 0.03	$0.023^{+0.003}_{-0.002}$	235.32/250
0803990201	$0.242^{+0.014}_{-0.013}$	$0.319^{+0.02}_{-0.019}$	$4.2^{+1.7}_{-1.2}$	$1.36^{+0.03}_{-0.02}$	0.028 ± 0.002	336.86/260
0803990301	$0.176^{+0.013}_{-0.012}$	$0.40^{+0.03}_{-0.02}$	$1.6^{+0.5}_{-0.4}$	$1.84^{+0.17}_{-0.14}$	$0.0031^{+0.0012}_{-0.0009}$	242.51/183
0803990401	$0.177^{+0.016}_{-0.014}$	0.46 ± 0.04	$0.46^{+0.2}_{-0.14}$	$2.0^{+0.3}_{-0.2}$	$0.0014^{+0.0009}_{-0.0006}$	173.38/176
0803990701	0.19 ± 0.03	0.359 ± 0.04	$2.7^{+2}_{-1.1}$	$2.0^{+0.3}_{-0.2}$	$0.0024^{+0.0017}_{-0.0011}$	95.21/71
0803990501	0.23 ± 0.02	0.29 ± 0.03	$4.1^{+3}_{-1.6}$	1.11 ± 0.04	0.0230 ± 0.004	185.33/185
0803990601	$0.198^{+0.016}_{-0.015}$	0.34 ± 0.03	$2.1^{+1.1}_{-0.7}$	$1.15^{+0.05}_{-0.04}$	0.023 ± 0.004	217.35/201

Notes: Parameter uncertainties were estimated at 68%.

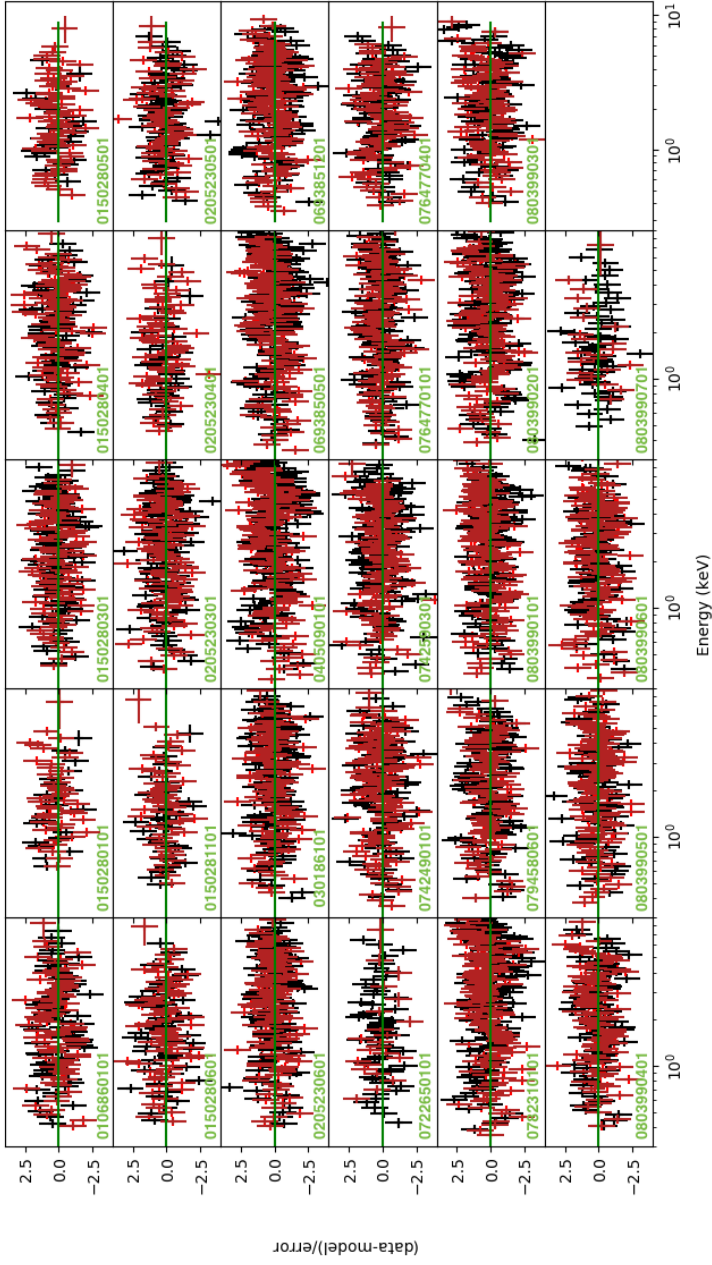


Fig. B.1: Spectral residuals for the 29 spectra extracted from NGC 1313 X-2, calculated with respect to the DISKBB+DISKBB model. Black and red points show data from the *XMM-Newton* EPIC-pn and EPIC-MOS detectors, respectively.

Appendix C: Table of fractional variability, F_{var}

Table C.1: Fractional variability (%) measured using 40 ks EPIC-pn segments of light curve for each observation, which is a common time baseline for comparing the RMS estimated.

Obs.ID	1st segment (40ks)	2nd segment (40/80ks)	3rd segment (80/120ks)
0106860101	-	-	-
0150280101	-	-	-
0150280301	-	-	-
0150280401	-	-	-
0150280501	-	-	-
0150280601	-	-	-
0150281101	-	-	-
0205230301	-	-	-
0205230401	-	-	-
0205230501	-	-	-
0205230601	-	-	-
0301860101	-	-	-
0405090101	10.98 ± 0.02	7.191 ± 0.012	-
0693850501	18.22 ± 0.04	17.05 ± 0.05	-
0693851201	2.245 ± 0.008	-	-
0722650101	-	-	-
0742590301	23.79 ± 0.07	-	-
0742490101	4.16 ± 0.04	5.616 ± 0.011	-
0764770101	3.463 ± 0.002	-	-
0764770401	-	-	-
0782310101	11.98 ± 0.04	24.53 ± 0.07	-
0794580601	-	-	-
0803990101	15.90 ± 0.02	9.333 ± 0.009	19.73 ± 0.03
0803990201	4.907 ± 0.003	21.97 ± 0.09	11.92 ± 0.02
0803990301	3.12 ± 0.04	-	-
0803990401	5.743 ± 0.004	-	-
0803990701	-	-	-
0803990501	18.87 ± 0.04	3.82 ± 0.15	-
0803990601	14.36 ± 0.10	-	-

Appendix D: Table DISKBB+DISKBB parameters with fixed N_H

Table D.1 reports the results of the spectral fits with the DISKBB+DISKBB model with fixed N_H ($N_H = (0.194 \times 10^{22}) \text{ cm}^{-2}$) for all *XMM-Newton* observations of X-2.

Table D.1: Best fitting spectral parameters of NGC1313 X-2 in different observations obtained with the absorbed DISKBB+DISKBB model with fixed N_H .

ObsID	N_H (10^{22} cm^{-2})	T_1 (keV)	norm ₁	T_2 (keV)	norm ₂	χ^2/dof
0106860101	0.194	0.348 ± 0.011	$2.9^{+0.4}_{-0.3}$	$1.85^{+0.14}_{-0.12}$	$0.0029^{+0.0009}_{-0.0007}$	149.22/146
0150280101	0.194	$0.22^{+0.06}_{-0.04}$	14^{+25}_{-9}	$1.38^{+0.09}_{-0.08}$	$0.037^{+0.005}_{-0.009}$	65.24/65
0150280301	0.194	$0.34^{+0.03}_{-0.02}$	$2.4^{+0.7}_{-0.5}$	$1.87^{+0.07}_{-0.06}$	$0.0141^{+0.0020}_{-0.0019}$	161.42/193
0150280401	0.194	$0.37^{+0.04}_{-0.03}$	$2.4^{+0.7}_{-0.5}$	$1.96^{+0.10}_{-0.09}$	0.014 ± 0.003	168.43/160
0150280501	0.194	0.35 ± 0.03	$3.5^{+1.5}_{-1.0}$	$1.53^{+0.18}_{-0.14}$	$0.0121^{+0.006}_{-0.005}$	90.97/89
0150280601	0.194	0.351 ± 0.02	$2.8^{+0.7}_{-0.5}$	$1.39^{+0.11}_{-0.09}$	0.0126 ± 0.004	157.44/124
0150281101	0.194	0.30 ± 0.02	$4.9^{+1.6}_{-1.2}$	$1.39^{+0.14}_{-0.11}$	$0.011^{+0.005}_{-0.004}$	69.78/84
0205230301	0.194	0.42 ± 0.03	$1.4^{+0.4}_{-0.3}$	1.89 ± 0.06	0.016 ± 0.002	220.15/212
0205230401	0.194	$0.305^{+0.016}_{-0.015}$	$4.6^{+1.1}_{-0.9}$	$1.86^{+0.2}_{-0.19}$	$0.0027^{+0.0014}_{-0.0010}$	88.11/92
0205230501	0.194	$0.341^{+0.013}_{-0.012}$	$3.1^{+0.5}_{-0.4}$	$1.75^{+0.14}_{-0.12}$	$0.0037^{+0.0013}_{-0.0010}$	143.70/130
0205230601	0.194	0.365 ± 0.03	$2.0^{+0.6}_{-0.5}$	$1.97^{+0.07}_{-0.06}$	$0.0131^{+0.0017}_{-0.0016}$	182.19/215
0301860101	0.194	0.44 ± 0.03	$1.0^{+0.3}_{-0.2}$	1.82 ± 0.06	0.016 ± 0.002	216.03/220
0405090101	0.194	0.432 ± 0.012	$1.38^{+0.12}_{-0.13}$	1.981 ± 0.04	0.0106 ± 0.0008	414.11/302
0693850501	0.194	0.386 ± 0.011	$1.60^{+0.16}_{-0.15}$	$1.434^{+0.019}_{-0.018}$	0.0273 ± 0.0016	314.18/286
0693851201	0.194	0.354 ± 0.009	$2.15^{+0.2}_{-0.18}$	1.12 ± 0.02	0.030 ± 0.003	271.48/237
0722650101	0.194	$0.315^{+0.016}_{-0.015}$	$3.1^{+0.7}_{-0.6}$	$2.9^{+0.7}_{-0.4}$	$0.0005^{+0.0004}_{-0.0003}$	64.17/74
0742590301	0.194	$0.398^{+0.017}_{-0.016}$	$1.42^{+0.2}_{-0.18}$	1.39 ± 0.03	0.025 ± 0.003	303.95/233
0742490101	0.194	$0.368^{+0.017}_{-0.016}$	$1.12^{+0.18}_{-0.16}$	1.238 ± 0.04	0.016 ± 0.002	232.48/199
0764770101	0.194	0.308 ± 0.005	3.7 ± 0.3	2.27 ± 0.09	0.0012 ± 0.0002	182.73/229
0764770401	0.194	0.36 ± 0.02	$2.1^{+0.5}_{-0.4}$	$1.14^{+0.06}_{-0.05}$	$0.030^{+0.007}_{-0.006}$	188.30/169
0782310101	0.194	$0.393^{+0.009}_{-0.008}$	$1.95^{+0.16}_{-0.14}$	1.870 ± 0.03	0.0099 ± 0.0007	381.64/292
0794580601	0.194	0.368 ± 0.016	2.5 ± 0.4	$1.55^{+0.07}_{-0.06}$	$0.013^{+0.003}_{-0.002}$	214.05/189
0803990101	0.194	0.398 ± 0.014	$1.14^{+0.14}_{-0.12}$	1.335 ± 0.03	0.021 ± 0.002	236.22/251
0803990201	0.194	$0.414^{+0.015}_{-0.014}$	$1.13^{+0.13}_{-0.11}$	1.43 ± 0.03	$0.0220^{+0.0019}_{-0.0018}$	354.12/261
0803990301	0.194	0.370 ± 0.011	$2.3^{+0.3}_{-0.2}$	$1.73^{+0.11}_{-0.10}$	$0.0041^{+0.0011}_{-0.0009}$	244.50/184
0803990401	0.194	0.370 ± 0.011	0.422 ± 0.018	$0.69^{+0.11}_{-0.09}$	$1.85^{+0.16}_{-0.13}$	174.49/177
0803990701	0.194	$0.357^{+0.019}_{-0.018}$	$2.8^{+0.6}_{-0.5}$	$2.0^{+0.3}_{-0.2}$	$0.0025^{+0.0014}_{-0.0010}$	95.22/72
0803990501	0.194	$0.344^{+0.018}_{-0.014}$	$1.8^{+0.3}_{-0.2}$	1.16 ± 0.04	0.018 ± 0.003	188.71/186
0803990601	0.194	0.346 ± 0.014	$1.9^{+0.3}_{-0.2}$	$1.16^{+0.04}_{-0.03}$	0.022 ± 0.003	217.43/202

Notes: Parameter uncertainties were estimated at 68%.